



# Persian buttercup-like $\text{BiOBr}_x\text{Cl}_{1-x}$ solid solution for photocatalytic overall $\text{CO}_2$ reduction to CO and $\text{O}_2$



Meichao Gao<sup>a</sup>, Jinxiang Yang<sup>a</sup>, Tao Sun<sup>a</sup>, Zizhong Zhang<sup>a,\*</sup>, Dafeng Zhang<sup>b</sup>, Huijuan Huang<sup>a</sup>, Huaxiang Lin<sup>a</sup>, Yi Fang<sup>c</sup>, Xuxu Wang<sup>a,\*</sup>

<sup>a</sup> State Key Laboratory of Photocatalysis on Energy and Environment, Research Institute of Photocatalysis, College of Chemistry, Fuzhou University, Fuzhou 350108, PR China

<sup>b</sup> School of Materials Science and Engineering, Liaocheng University, Liaocheng, Shandong 252000, PR China

<sup>c</sup> School of Materials Science and Engineering, Fuzhou University, Fuzhou 350108, PR China

## ARTICLE INFO

**Keywords:**  
 $\text{BiOBr}_x\text{Cl}_{1-x}$   
 Solid solution  
 Photocatalysis  
 $\text{CO}_2$  conversion

## ABSTRACT

The photocatalytic overall conversion of  $\text{CO}_2$  with  $\text{H}_2\text{O}$  to chemical fuel and oxygen mimicking natural photosynthesis is a huge challenge in photocatalysis. This work shows the achievement of the solar-driven photocatalytic overall  $\text{CO}_2$  reduction with  $\text{H}_2\text{O}$  to CO and  $\text{O}_2$  over a Persian buttercup-like  $\text{BiOBr}_x\text{Cl}_{1-x}$  solid solution. A CO generation rate of  $15.86 \mu\text{mol g}^{-1}\text{h}^{-1}$  with the approximate stoichiometric  $\text{O}_2$  evolution is yielded on  $\text{BiOBr}_{0.6}\text{Cl}_{0.4}$  solid solution under simulated solar light irradiation, which was about 7.5 and 10.2 times higher than that of pure  $\text{BiOCl}$  ( $2.11 \mu\text{mol g}^{-1}\text{h}^{-1}$ ) and  $\text{BiOBr}$  ( $1.55 \mu\text{mol g}^{-1}\text{h}^{-1}$ ), respectively. The enhanced photoactivity is contributed to the mediate band gap and energy level tuned by the formation of  $\text{BiOBr}_x\text{Cl}_{1-x}$  solid solution to facilitate the separation of photogenerated charges. Besides the unique electron structure, the photoinduced oxygen vacancy ( $\text{O}_v$ ) formed on  $\text{BiOBr}_x\text{Cl}_{1-x}$  solid solution also plays an important role in the  $\text{CO}_2$  reduction.

## 1. Introduction

The ever-increasing worldwide consumption of fossil fuels has accelerated the depletion of these finite natural resources and led to overproduction of the greenhouse gas carbon dioxide [1–4]. Reduction of the overly produced  $\text{CO}_2$  into reusable carbon forms is idea solution to carbon cycling [5,6]. Among many different approaches developed for  $\text{CO}_2$  reactivation, the photocatalytic reduction of  $\text{CO}_2$  has been widely studied due to its sustainable and low-cost feature [7–10]. Theoretically, the photooxidation of  $\text{H}_2\text{O}$  into  $\text{O}_2$  is indispensable to accompany with the  $\text{CO}_2$  photocatalytic reduction process, unless the electron donor was sacrificed to replace the  $\text{H}_2\text{O}$  oxidation [11]. When the reduction reactions occur in the presence of sacrificial electron donor reagents, it may not be a real solar energy-to-fuel conversion from the perspective of both thermodynamics and practical application [12]. Undoubtedly, the pursuing objective is the overall conversion of  $\text{CO}_2$  with  $\text{H}_2\text{O}$  to fuel and oxygen rather than the simple conversion with the aid of a sacrificial reagent by photocatalysis, but still remains a huge challenge in photocatalysis.

Recently, bismuth oxyhalide ( $\text{BiOX}$ , X = Cl, Br, and I) materials can be capable for  $\text{CO}_2$  photoreduction [13–16].  $\text{BiOCl}$  sheets with highly

exposed {001} facets exhibited a high activity for photocatalytic reduction of  $\text{CO}_2$  to  $\text{CH}_4$  [17]. However, the  $\text{BiOCl}$  photocatalyst is only active upon UV excitation because of its large energy band of  $\sim 3.2 \text{ eV}$  [18], which seriously limits the utilization of solar energy. Although the  $\text{BiOBr}$  or  $\text{BiOI}$  extends the optical absorption to visible light for more efficiently harvesting solar energy, the relatively low conduction band minimum (CBM) energy of  $\text{BiOBr}$  and  $\text{BiOI}$  results in no sufficient potential energy to induce the  $\text{CO}_2$  reduction [19], and thus the  $\text{CO}_2$  photocatalytic conversion is difficult over  $\text{BiOBr}$  and  $\text{BiOI}$ . Therefore, the realization of highly efficient  $\text{CO}_2$  photocatalytic conversion by harvesting solar energy over  $\text{BiOX}$  materials are still major hindrance that needs to be overcome. The integration of  $\text{BiOCl}$  with high  $\text{CO}_2$  photocatalytic conversion and  $\text{BiOBr}$  with efficient visible-light absorption into one photocatalyst may be a feasible approach for solving problems. Moreover, different halogen  $\text{BiOX}$  possesses a similar crystal structure to make the halogen facilely substitute each other to form a solid solution photocatalyst.

In this work, a nanostructure Persian buttercup-like  $\text{BiOBr}_x\text{Cl}_{1-x}$  solid-solution were prepared by a facile precipitation method without adding any organic template. The formation of solid solutions leads to well tuning the band gap, and local electronic structure of the

\* Corresponding authors.

E-mail addresses: [z.zhang@fzu.edu.cn](mailto:z.zhang@fzu.edu.cn) (Z. Zhang), [xwang@fzu.edu.cn](mailto:xwang@fzu.edu.cn) (X. Wang).

photocatalyst, and thus improves the photocatalytic activities of  $\text{CO}_2$  conversion. The optimal  $\text{BiOBr}_{0.6}\text{Cl}_{0.4}$  delivers an excellent photocatalytic  $\text{CO}_2$  reduction with water vapor towards a CO generation rate of  $15.86 \mu\text{mol g}^{-1} \text{h}^{-1}$  without using any organic scavengers or noble metal cocatalysts, which was about 7.5 and 10.2 times larger than that of pure  $\text{BiOCl}$  ( $2.11 \mu\text{mol g}^{-1} \text{h}^{-1}$ ) and  $\text{BiOBr}$  ( $1.55 \mu\text{mol g}^{-1} \text{h}^{-1}$ ), respectively. Meanwhile, the approximate stoichiometric  $\text{O}_2$  was produced. This work provides not only insights into the rational design of  $\text{BiOX}$  ( $X = \text{Cl}$  and  $\text{Br}$ ) photocatalysts for  $\text{CO}_2$  reduction, but also a mechanism of photocatalytic  $\text{CO}_2$  reduction on  $\text{BiOBr}_{x}\text{Cl}_{1-x}$  solution photocatalyst.

## 2. Experimental section

All the chemical reagents were of analytical grade and purchased from Aladdin Industrial Corporation without further purification before use. Deionized water was used throughout the work.

### 2.1. Preparation of $\text{BiOBr}_{x}\text{Cl}_{1-x}$

$\text{BiOBr}_{x}\text{Cl}_{1-x}$  photocatalysts were synthesized via a simple precipitation method. First, 0.02 mol bismuth nitrate pentahydrate ( $\text{Bi}(\text{NO}_3)_3 \cdot 5\text{H}_2\text{O}$ ) and 2 mL concentrated nitric acid was dissolved in 20 mL deionized water under vigorous stirring to obtain a transparency liquid. In addition, 0.02 mol ammonium halide ( $\text{NH}_4\text{Br}/\text{NH}_4\text{Cl} = 0, 0.2, 0.4, 0.6, 0.8, 1$ ) were dissolved in 20 mL deionized water, and the obtained solution was added quickly into the above  $\text{Bi}(\text{NO}_3)_3$  solution. After 2 h stirring, the suspension was centrifuged at 5000 rpm. The white precipitate was collected by centrifugation, rinsed thoroughly with deionized water, and dried at 333 K in the air. Then the mixture was finally calcined at 573 K for 1 h in air atmosphere.

### 2.2. Characterization

X-ray diffraction (XRD) patterns were recorded on a diffractometer (D8 Advanced, Bruker Co., Germany) with  $\text{Cu K}\alpha$ -radiation operated at 40 kV and 40 mA. The data were recorded in a 2 $\theta$  range of 15–75° with a step width of 0.02. Scanning (SEM) and transmission electron microscopy (TEM) was performed with a JSM-6700 F microscope equipped with an energy-dispersive X-ray spectrometer (EDS) and a JEM-2100 microscope (JEOL Ltd., Japan), respectively. The Brunauer–Emmett–Teller (BET) specific surface area of the samples was characterized on a Quantachrome Autosorb IQ-C nitrogen adsorption apparatus (Quantachrome Co., USA). Ultraviolet–visible (UV–vis) diffuse reflectance spectra (DRS) of samples and the absorption spectra of RhB were recorded on a UV-3600 spectrophotometer (Shimadzu, Japan). Photoluminescence (PL) spectra of samples were recorded with an FLS 920 Fluorescence and Phosphorescence spectrometer (Edinburgh Instruments Ltd.) with  $\lambda_{\text{ex}} = 320 \text{ nm}$ . The elemental composition of samples was analyzed by X-ray photoelectron spectroscopy (XPS, VG, Physical Electrons Quantum 2000 Scanning Esca Microprob, Al K1 radiation). The products of the  $^{18}\text{O}_2$  and  $^{16}\text{O}_2$  isotopic experiment were analyzed by Hiden HPR-20 mass spectrometer. Electron paramagnetic resonance (EPR) spectra were recorded with a Bruker EPR A200 spectrometer with a microwave frequency of 9.5 GHz.

### 2.3. Photocatalytic $\text{CO}_2$ conversion

Photocatalytic reduction of  $\text{CO}_2$  in the presence of  $\text{H}_2\text{O}$  was carried out as a gas–solid heterogeneous reaction in a 40 mL Schlenk flask with a silicone rubber septum under atmospheric pressure at ambient temperature (298 K). A xenon lamp (300D, Perfectlight, China) with a focus intensity of  $0.2 \text{ W cm}^{-2}$  was used to simulate sunlight. 10 mg of photocatalyst was placed into the reaction tube. Then, this system was evacuated by a mechanical pump and filled with pure  $\text{CO}_2$  gas. This evacuation–filling operation was repeated three times. Finally, 20  $\mu\text{L}$  of

pure water was introduced into the reactor via the silicone rubber septum. The photocatalytic reaction was typically performed for 3 h, while the stability test was performed 4 h per cycle. The reaction system was evacuated after each 4 h and refilled with  $\text{CO}_2$  and pure water. After the irradiation, the production amount of CO,  $\text{CH}_4$ ,  $\text{H}_2$  and  $\text{O}_2$  was analyzed using the Agilent GC-7890B gas chromatograph equipped with a FID detector, a TCD detector and a chromatographic column (TDX-01).

### 2.4. Photoelectrochemical measurement

Photoelectrochemical measurements were carried out with a BAS Epsilon workstation using a standard three-electrode electrochemical cell with a working electrode, a platinum foil as the counter electrode, and a saturated  $\text{Ag}/\text{AgCl}$  electrode as the reference. A sodium sulfate solution (0.2 M) was used as the electrolyte. The working electrode was prepared by FTO glass pieces, which was cleaned by sonication in cleanout fluid, acetone and ethanol in sequence. The photocatalyst was dispersed in ethanol under sonication to form a suspension. A photocatalyst film was fabricated by spreading the suspension onto the conductive surface of the FTO glass. Periodic photocurrent response was measured by introducing a 300 W Xe lamp as the light source. Mott–Schottky experiments were also carried out with the three-electrode system. The potential window ranged from  $-1$  to  $0 \text{ eV}$ , and the perturbation signal was 10 mV with the frequencies at 0.5, 1.0, and 1.5 KHz, respectively.

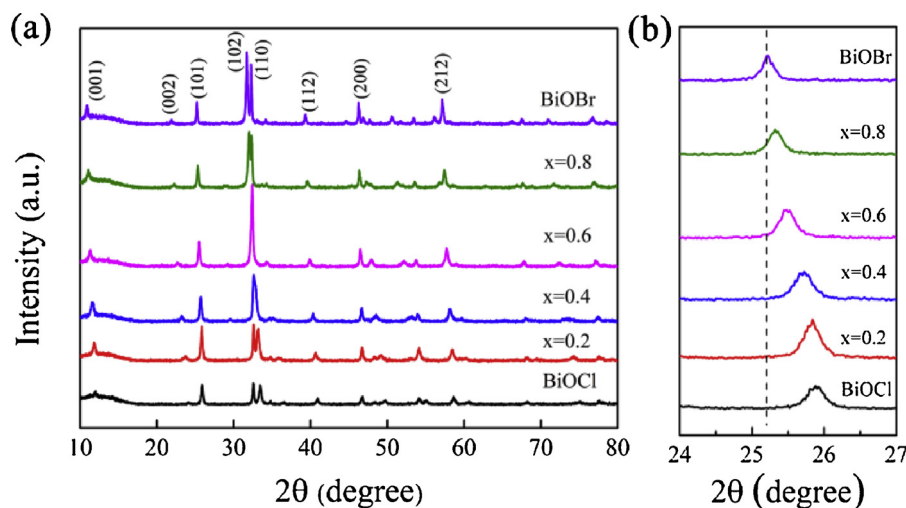
## 3. Results and discussion

### 3.1. Crystal structure, morphology and surface characteristics

Fig. 1 shows the XRD patterns of the as-prepared samples  $\text{BiOCl}$ ,  $\text{BiOBr}_{x}\text{Cl}_{1-x}$  and  $\text{BiOBr}$ . The XRD peaks of the pristine  $\text{BiOBr}$  and  $\text{BiOCl}$  are in keeping with the standard XRD patterns of tetragonal  $\text{BiOBr}$  (JCPDS no. 09-0393) and tetragonal  $\text{BiOCl}$  (JCPDS no. 06-0249) [20,21]. The  $\text{BiOBr}_{x}\text{Cl}_{1-x}$  solid solutions display the similar XRD pattern with the pristine  $\text{BiOBr}$  and  $\text{BiOCl}$  due to similar tetragonal structures. The result indicates that  $\text{BiOBr}_{x}\text{Cl}_{1-x}$  is likely a good solid solution [22–24]. Fig. 1b displays the enlarged XRD patterns in the range of 20–30°. As the ratio of  $\text{Cl}^-$  increases to replace  $\text{Br}^-$  in  $\text{BiOBr}_{x}\text{Cl}_{1-x}$  solid solutions, the diffraction peaks at about 25.2° corresponding to (101) facets gradually shift toward higher 2 $\theta$  angles, owing to the smaller radius of  $\text{Cl}^-$  with respect to  $\text{Br}^-$  for shrinking atomic distance [23]. This reveals that  $\text{BiOBr}_{0.2}\text{Cl}_{0.8}$ ,  $\text{BiOBr}_{0.4}\text{Cl}_{0.6}$ ,  $\text{BiOBr}_{0.6}\text{Cl}_{0.4}$ , and  $\text{BiOBr}_{0.8}\text{Cl}_{0.2}$  are definitely solid solutions rather than simple mixtures of  $\text{BiOBr}$  and  $\text{BiOCl}$ .

The morphologies of the as-prepared  $\text{BiOCl}$ ,  $\text{BiOBr}_{0.6}\text{Cl}_{0.4}$  and  $\text{BiOBr}$  samples were investigated by SEM, as shown in Fig. 2. The  $\text{BiOCl}$  sample appears in the form of microspheres with a diameter varied from 8 to 10  $\mu\text{m}$  (Fig. 2a–b). These microspheres are consisted of thin  $\text{BiOCl}$  nanosheets with the thickness of  $\sim 30 \text{ nm}$ .  $\text{BiOBr}_{0.6}\text{Cl}_{0.4}$  shows a Persian buttercup-like nanoflower morphology through stacking self-assembly of nanoplate subunit (Fig. 2c–e). Moreover, the hierarchical architecture of the Persian buttercup-like superstructures has a smaller dimension and a looser nanoplate array, as compared with the pristine  $\text{BiOCl}$  microspheres. The thickness of 38 nm for the nanoplates and 2.4  $\mu\text{m}$  in diameter of a single superstructure are shown in Fig. 2d. For  $\text{BiOBr}$ , the thinner nanosheets are assembled to a scattered flower-like structure (Fig. 2f).

The more detailed microstructures of  $\text{BiOBr}_{0.6}\text{Cl}_{0.4}$  samples were furthermore revealed by TEM. The TEM images (Fig. 3) show clearly the different microsphere morphology of  $\text{BiOCl}$ ,  $\text{BiOBr}_{0.6}\text{Cl}_{0.4}$  and  $\text{BiOBr}$ , which are in agreement with the SEM images. The great contrast of brightness and darkness between  $\text{BiOCl}$  and  $\text{BiOBr}_{0.6}\text{Cl}_{0.4}$  clearly demonstrates the loose structure of  $\text{BiOBr}_{0.6}\text{Cl}_{0.4}$  nanoflower, which is advantageous to the reactant adsorption and mass transfer and thus

Fig. 1. XRD patterns of  $\text{BiOBr}_x\text{Cl}_{1-x}$ .

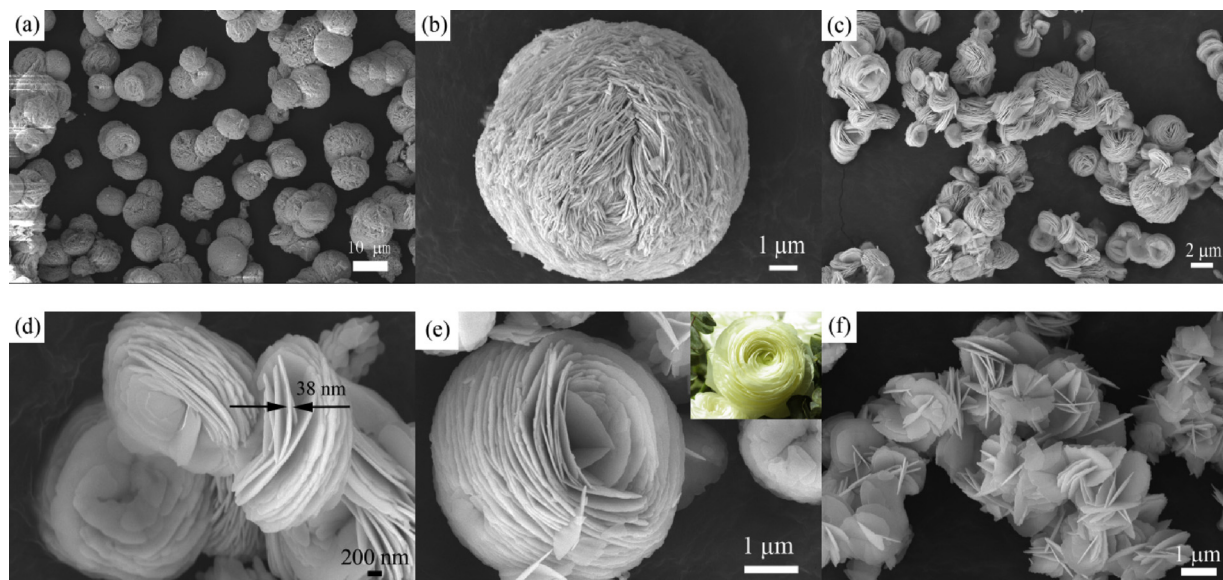
results in a high photocatalytic activity of the nanoflowers. The high-resolution TEM (HRTEM) images (Fig. 3a,b inset) reveal lattice fringes with a  $d$ -spacing of 0.735 and 0.811 nm, which match with the {001} plane of  $\text{BiOCl}$  and  $\text{BiOBr}$ , respectively [25,26]. For  $\text{BiOBr}_{0.6}\text{Cl}_{0.4}$  solid solution, HRTEM image (Fig. 3c inset) reveals highly crystalline and clear lattice fringes with an interplanar lattice spacing of 0.780 nm, which falls in between that of  $\text{BiOCl}$  and  $\text{BiOBr}$ . This further confirms that  $\text{BiOBr}_x\text{Cl}_{1-x}$  samples are solid solutions. As shown in Fig. 3d, the elemental mapping shows that the elements are uniformly distributed in  $\text{BiOBr}_{0.4}\text{Br}_{0.6}$  nanoflower. The EDX spectra (Fig. S1) shows that as-obtained  $\text{BiOBr}_{0.6}\text{Cl}_{0.4}$  photocatalyst is composed of the elements Bi, O, Br, and Cl. The molar ratio of Br/Cl in the  $\text{BiOBr}_{0.6}\text{Cl}_{0.4}$  is 1.5, which is well consistent with the expected value in the experiment. The BET method has been used to characterize the surface areas. Results are shown in Table S2. The BET specific surface areas of  $\text{BiOCl}$ ,  $\text{BiOBr}_{0.6}\text{Cl}_{0.4}$  and  $\text{BiOBr}$  are calculated to be  $5.44 \text{ m}^2 \text{ g}^{-1}$ ,  $14.53 \text{ m}^2 \text{ g}^{-1}$  and  $59.75 \text{ m}^2 \text{ g}^{-1}$ , respectively.

The surface chemical compositions and oxidation states of the  $\text{BiOBr}_{0.6}\text{Cl}_{0.4}$  were analyzed by XPS. A full survey scan spectrum (Fig. S2) indicates the presence of Bi, O, Br, and Cl in the  $\text{BiOBr}_{0.6}\text{Cl}_{0.4}$ . The Br/Cl atomic ratio calculated from the XPS data by measuring the ratio

of the Br and Cl peak areas is determined to be 1.58, further confirming the composition of  $\text{BiOBr}_{0.6}\text{Cl}_{0.4}$ . In the high-resolution XPS spectra of O1s (Fig. S3), besides the main Bi–O peak at 531.3 eV, another peak appearing at 533.7 eV is attributed to the surface hydroxyl groups on  $\text{BiOBr}_{0.6}\text{Cl}_{0.4}$  [27]. Fig. 4 shows a high-resolution XPS spectrum of the Bi 4f of the as-prepared  $\text{BiOBr}$ ,  $\text{BiOBr}_{0.6}\text{Cl}_{0.4}$  and  $\text{BiOCl}$ . For  $\text{BiOBr}$ , the binding energies at 158.9 and 164.2 eV are ascribed to  $\text{Bi} 4f_{7/2}$  and  $\text{Bi} 4f_{5/2}$ , respectively [28]. And for  $\text{BiOCl}$ , the binding energies at 159.6 and 164.9 eV are attributed to  $\text{Bi}^{3+} 4f_{7/2}$  and  $\text{Bi}^{3+} 4f_{5/2}$ , respectively [15]. Obviously, there are two different oxidation states for  $\text{Bi}^{3+}$  in solid solution  $\text{BiOBr}_{0.6}\text{Cl}_{0.4}$ , corresponding to that of  $\text{Bi}^{3+}$  in  $\text{BiOBr}$  and  $\text{BiOCl}$ , respectively.

### 3.2. Optical properties, band structures and enhancement analysis

As key factors governing their photocatalytic activity, the optical absorption properties of the semiconductor photocatalyst are relevant to the electronic structure features [29–31]. The UV–vis diffuse reflectance spectra of  $\text{BiOBr}_x\text{Cl}_{1-x}$  samples are shown in Fig. 5a.  $\text{BiOCl}$  and  $\text{BiOBr}$  exhibit a sharp absorption edge respectively at 380 and 440 nm due to the band gap transition [32,33]. As expected,  $\text{BiOBr}_x\text{Cl}_{1-x}$

Fig. 2. SEM image of (a) (b)  $\text{BiOCl}$ ; (c) (d) (e)  $\text{BiOBr}_{0.6}\text{Cl}_{0.4}$  and (f)  $\text{BiOBr}$ .

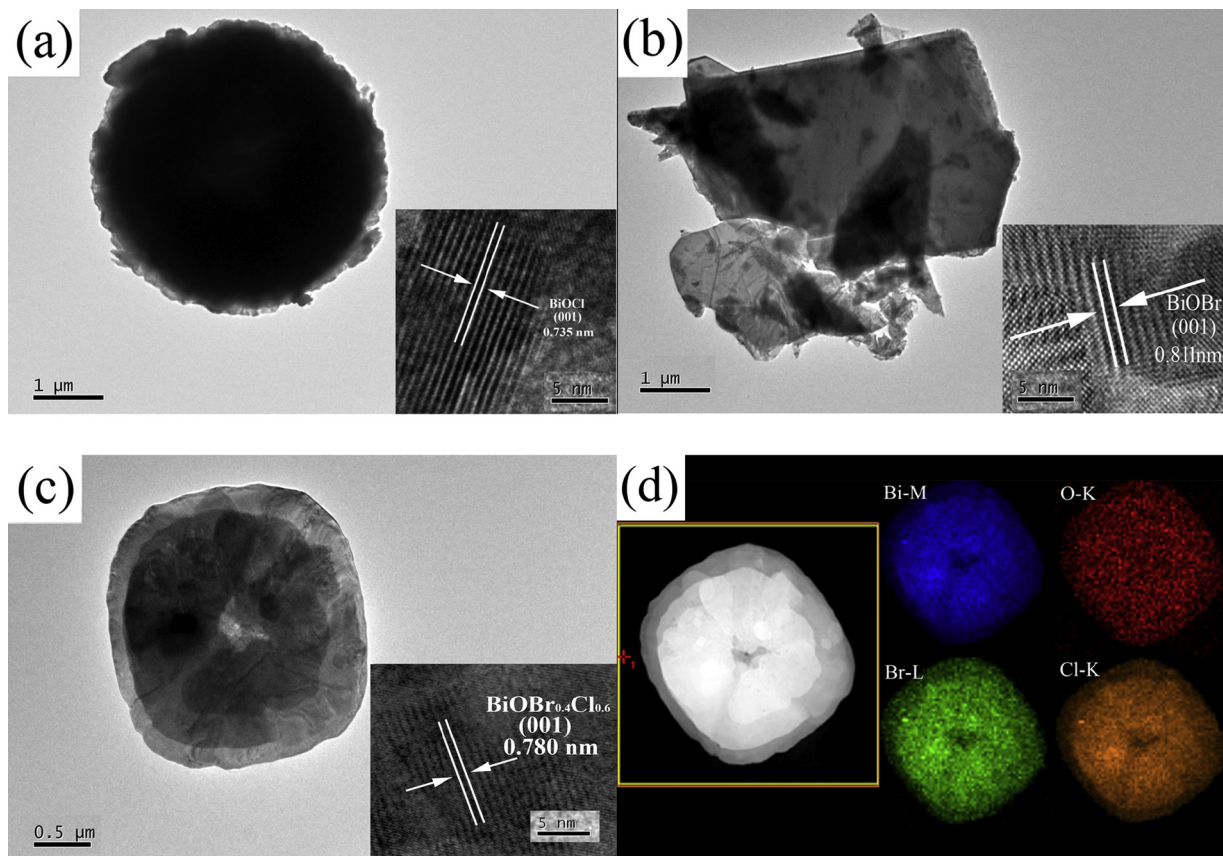


Fig. 3. TEM and HRTEM images inset: (a) BiOCl; (b) BiOBr and (c) BiOBr<sub>0.6</sub>Cl<sub>0.4</sub>; (d) EDX mapping images of Bi, O, Br and Cl, respectively.

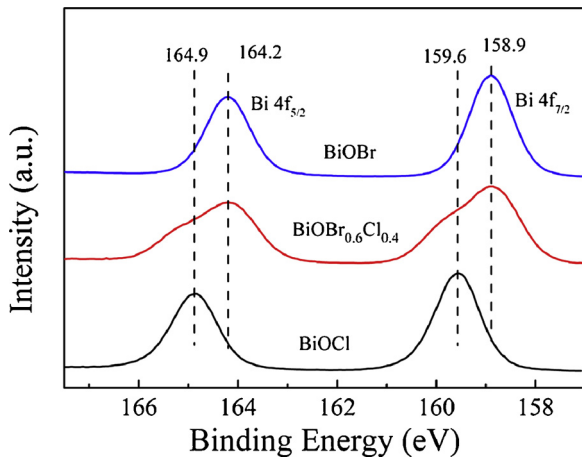


Fig. 4. XPS Bi 4f spectra of the as-prepared BiOBr, BiOBr<sub>0.6</sub>Cl<sub>0.4</sub> and BiOCl.

displays a broader photoabsorption from the UV to the visible light region as the Br<sup>-</sup> ion content increases [34]. The optical band gap is calculated to be about 3.2, 2.99, 2.85, 2.79, 2.71, and 2.60 eV for BiOBr<sub>x</sub>Cl<sub>1-x</sub> (x = 0, 0.2, 0.4, 0.6, 0.8, 1), respectively (Fig. S6).

To examine and confirm the optical properties of BiOBr<sub>x</sub>Cl<sub>1-x</sub>, Mott–Schottky measurements were taken at various frequencies of 1.5 KHz, 1.0 KHz and 0.5 KHz, respectively. The positive slope of the Mott–Schottky plots indicate that they are n-type semiconductors, as shown in Fig. S7 [35,36]. The flat band potentials of BiOCl, BiOBr<sub>0.6</sub>Cl<sub>0.4</sub> and BiOBr can be determined by extrapolating the lines to  $1/C^2 = 0$ , and are found to be -1.22 V, -0.80 V and -0.34 V (vs. Ag/AgCl), respectively. As is known to all, for n-type semiconductors, the flat potential is equal to the CB position [13,37], whereby the CB

potential of BiOCl, BiOBr<sub>0.6</sub>Cl<sub>0.4</sub> and BiOBr are -1.22 V, -0.80 V and -0.34 V, respectively. The data of electron structures of three semiconductor components are illustrated together in Fig. 5b. Although BiOBr<sub>0.6</sub>Cl<sub>0.4</sub> has more positive CB position than BiOCl, it is still thermodynamically accessible for CO<sub>2</sub> conversion to CO directly.

To evaluate the photoinduced charge separation and transfer efficiency of the samples, electrochemical measurements were performed in a three-electrode electrochemical setup [38,39]. As shown in Fig. 5c, the photocurrent of the BiOBr<sub>0.6</sub>Cl<sub>0.4</sub> electrode is significantly higher than that of the BiOCl or BiOBr electrode. The lower recombination and superior separation of the photogenerated charge carriers of BiOBr<sub>0.6</sub>Cl<sub>0.4</sub> solid solution were also confirmed by PL spectra [40]. BiOBr<sub>0.6</sub>Cl<sub>0.4</sub> displays a much lower PL intensity compared with BiOBr and BiOCl, as shown in Fig. 5d. Hence, the more efficient photoinduced electron–hole separation and electron transfer of BiOBr<sub>0.6</sub>Cl<sub>0.4</sub> are beneficial for the CO<sub>2</sub> photoreduction process [41–43].

### 3.3. Photocatalytic reduction of CO<sub>2</sub>

The photocatalytic reduction of CO<sub>2</sub> over the samples was performed under simulated solar light irradiation in the presence of H<sub>2</sub>O vapor. CO was major product and only a trace amount of CH<sub>4</sub> and no H<sub>2</sub> was detected in the gas phase products (Fig. S8). The effect of light illumination on the photocatalytic activity was studied, as shown in Fig. S9. Obviously, when light off, the CO evolution on BiOBr<sub>0.6</sub>Cl<sub>0.4</sub> was greatly suppressed, implying that light illumination plays a great role in the photoreduction reaction of CO<sub>2</sub>. In addition, almost no CO was detected in the case of pumping with Ar after light irradiation for 4 h, indicating that CO came from the reduction of CO<sub>2</sub>, rather than catalyst or other sources of carbon. The photocatalytic rates of CO over BiOBr<sub>x</sub>Cl<sub>1-x</sub> (x = 0, 0.2, 0.4, 0.6, 0.8 and 1) solid solutions are shown in Fig. 6a. BiOBr<sub>0.6</sub>Cl<sub>0.4</sub> exhibited the best photocatalytic rate of 15.86

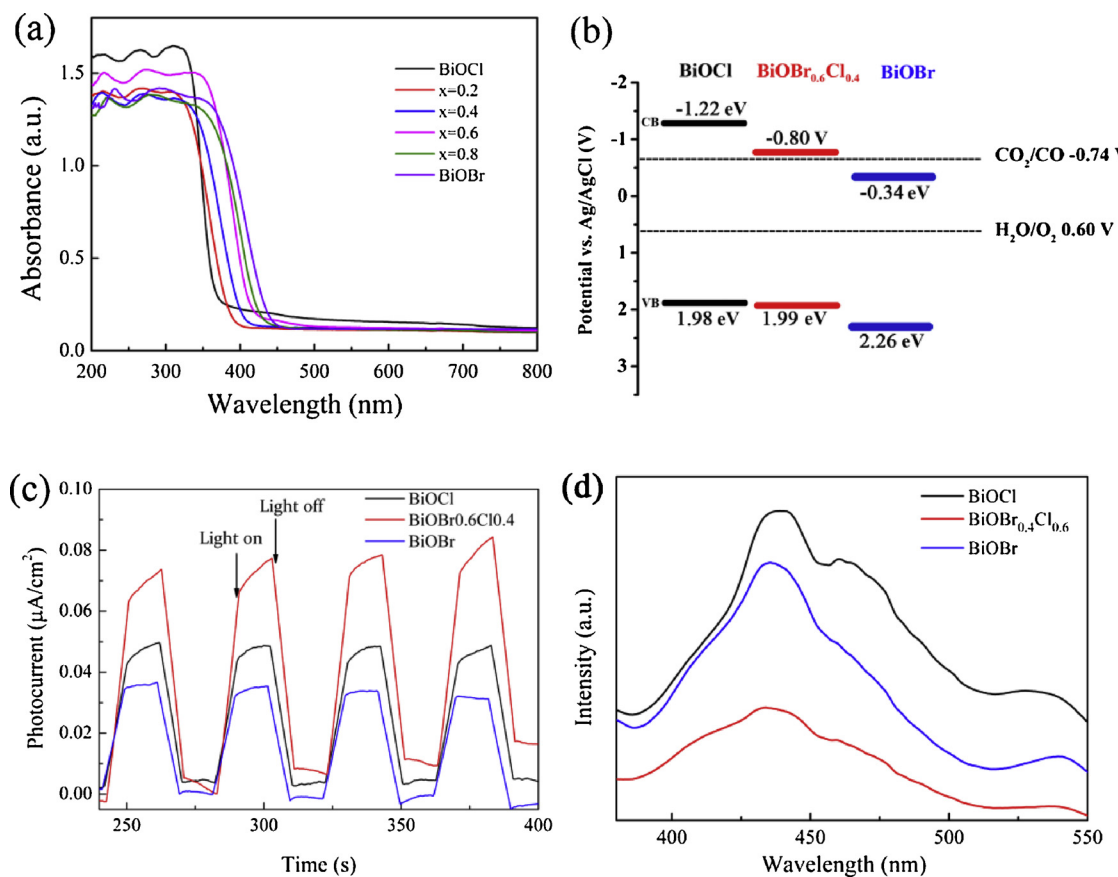


**Fig. 5.** (a) UV-vis DRS spectra of  $\text{BiOBr}_{x}\text{Cl}_{1-x}$ ; (b) Energy band structure of photocatalysts for the  $\text{CO}_2$  reduction to  $\text{CO}$ ; (c) photocurrent responses and (d) PL spectra of  $\text{BiOCl}$ ,  $\text{BiOBr}_{0.6}\text{Cl}_{0.4}$  and  $\text{BiOBr}$ .

$\mu\text{mol g}^{-1} \text{h}^{-1}$ , which was about 7.5 times larger than that of pure  $\text{BiOCl}$  ( $2.11 \mu\text{mol g}^{-1} \text{h}^{-1}$ ) and 10.2 times larger than that of pure  $\text{BiOBr}$  ( $1.55 \mu\text{mol g}^{-1} \text{h}^{-1}$ ). Furthermore,  $\text{BiOBr}_{0.6}\text{Cl}_{0.4}$  kept its high activity of the production rate of  $\text{CO}$  after 4 cycle reaction during total 16 h, as shown in Fig. 6b. No significant change in the photocatalytic activity and crystalline structure can be observed after 4 cycles.  $\text{CO}$  and  $\text{O}_2$  gas evolution in a stoichiometric ratio ( $\text{CO}:\text{O}_2 = 2:1$ ) has been detected over  $\text{BiOBr}_{0.6}\text{Cl}_{0.4}$  photocatalyst (Fig. 6c). Isotopic experiments using  $\text{H}_2^{18}\text{O}$  (Fig. S10) show that  $^{18}\text{O}_2$  was the main product of the reaction, as revealed by the peak at  $m/z = 36$ . This confirms the produced  $\text{O}_2$  resulting from  $\text{H}_2\text{O}$  oxidation. The effect of  $\text{H}_2\text{O}$  on the photocatalytic activity was also further studied. By using dry  $\text{CO}_2$  feed gas and reducing the water molecule adsorption on the sample surface as far as possible, the  $\text{CO}$  evolution on  $\text{BiOBr}_{0.6}\text{Cl}_{0.4}$  was greatly suppressed, as shown in Fig. S11. This implies that  $\text{H}_2\text{O}$  molecules played a great role in the photoreduction reaction of  $\text{CO}_2$ . It is believed that  $\text{CO}_2$  could

react with  $\text{H}_2\text{O}$  through two respective half reactions with photo-generated electrons and hole to simultaneously produce  $\text{CO}$  and  $\text{O}_2$  in an ideal process (Scheme S1).

It's worth noting that, the **white**  $\text{BiOBr}_{x}\text{Cl}_{1-x}$  samples gradually became grey and then grey-black during the light irradiation and became **white** again in the presence of water after 24 h, as shown in Fig. S13a. The interesting phenomenon is in line with the previous reported work [16,44], which is resulted from the generation and recovery of the oxygen vacancies ( $\text{O}_v$ ) in the  $\text{BiOX}$ . In order to investigate  $\text{O}_v$  formed in the  $\text{BiOBr}_{0.6}\text{Cl}_{0.4}$  sample after the light irradiation, EPR analysis was employed to explore the generated  $\text{O}_v$  in the  $\text{BiOBr}_{0.6}\text{Cl}_{0.4}$  sample during irradiation, as shown in Fig. 7. No obvious signal can be observed for the  $\text{BiOBr}_{0.6}\text{Cl}_{0.4}$  sample before light irradiation. A much stronger  $\text{O}_v$  signal at  $g = 2.001$  appeared under light irradiation for 1 h [45,46]. The  $\text{O}_v$  signal disappeared for the  $\text{BiOBr}_{0.6}\text{Cl}_{0.4}$  sample in the presence of water after 24 h. From the XRD spectrum (Fig. S13b), no

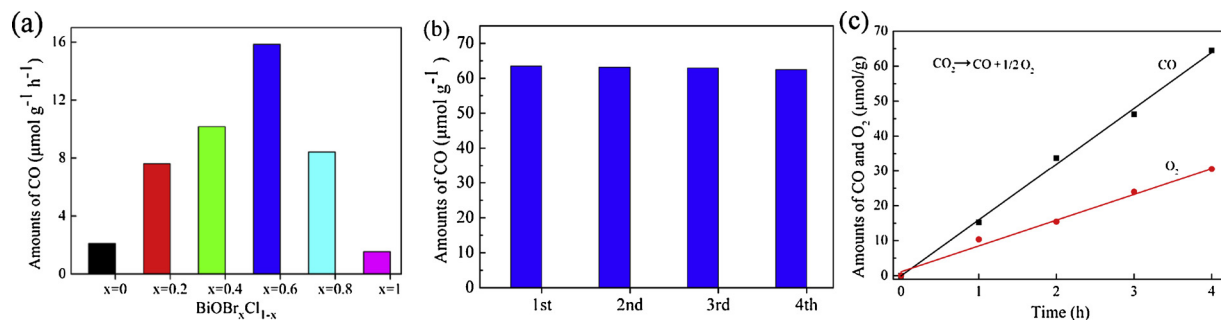


**Fig. 6.** (a) Rates of products for  $\text{BiOBr}_{x}\text{Cl}_{1-x}$ , (b) cyclic experiment over  $\text{BiOBr}_{0.6}\text{Cl}_{0.4}$  for 4 h per circulation and (c)  $\text{CO}$  and  $\text{O}_2$  evolution rate of  $\text{BiOBr}_{0.6}\text{Cl}_{0.4}$  under simulated solar light irradiation.

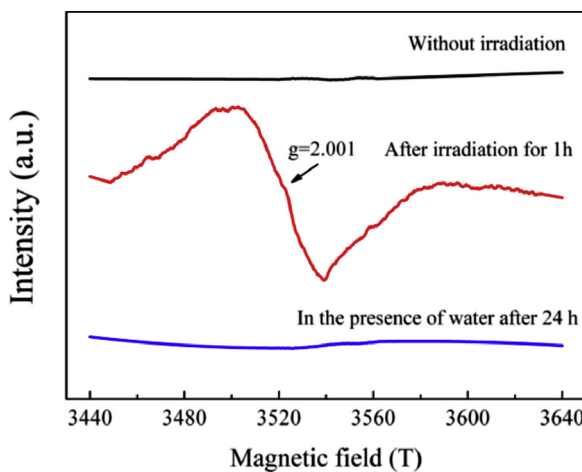
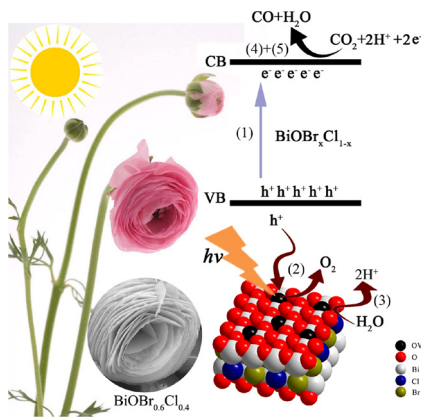


Fig. 7. EPR spectra of the as-prepared Persian buttercup-like  $\text{BiOBr}_{0.6}\text{Cl}_{0.4}$ .

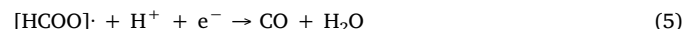
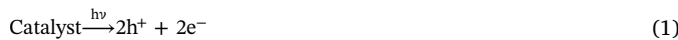


**Scheme 1.** Schematic illustrations of the proposed mechanism in the solid solution:  $\text{O}_v$  generated and consumed under simulated sunlight irradiation.

crystal structure variation could be found compared with the original one. The sample keeps its high activity of the production rate of CO (Fig.S14) further confirming the excellent reusability and stability.

#### 3.4. Photocatalytic mechanism

Based on the above understanding, the mechanism of photocatalytic  $\text{CO}_2$  reduction over the  $\text{BiOBr}_x\text{Cl}_{1-x}$  solid solution under simulated solar light irradiation is described as follows (Scheme 1): Under irradiation,  $\text{BiOBr}_x\text{Cl}_{1-x}$  is stimulated to form the photogenerated electrons ( $e^-$ ) and holes ( $h^+$ ). The  $h^+$  oxidize the lattice oxygen ( $\text{O}_2^-$ ) to form the oxygen defect ( $\text{O}_v$ ) and dioxygen ( $\text{O}_2$ ) [47]. The  $\text{O}_v$  activates  $\text{H}_2\text{O}$  molecule to recover  $\text{O}_v$  and generate ions ( $\text{H}^+$ ) [48].  $\text{CO}_2$  molecule captures one proton ( $\text{H}^+$ )-electron ( $e^-$ ) pair to transform into the carboxyl species  $[\text{HCOO}]^-$ , and then receives a second proton-electron pair to produce CO and  $\text{H}_2\text{O}$  [49,50]. It's worth noting that  $\text{H}_2\text{O}$  takes part in the photocatalytic process, but it gets recovery after the reaction. This is supported by the isotope tracer control experiment adding  $\text{H}_2^{18}\text{O}$  (Fig. S10), from which it can be seen that  $^{18}\text{O}_2$  instead of  $^{16}\text{O}_2$  is detected as a main product. Based on the above discussion, we concluded that the photocatalytic  $\text{CO}_2$  reduction process can be divided into the following steps:



where  $\text{h}^+$  represents the photogenerated hole in  $\text{BiOBr}_x\text{Cl}_{1-x}$ ,  $\text{e}^-$  represents the photoexcited electron in  $\text{BiOBr}_x\text{Cl}_{1-x}$ ,  $\text{O}_2^-$  represents the lattice oxygen of the  $\text{BiOBr}_x\text{Cl}_{1-x}$ ,  $\text{O}_v$  represents the oxygen vacancy in  $\text{BiOBr}_x\text{Cl}_{1-x}$  and  $[\text{HCOO}]^-$  represents the carboxyl radical. Therefore,  $\text{CO}_2$  could react with  $\text{H}_2\text{O}$  with photogenerated electrons and hole to simultaneously produce CO and  $\text{O}_2$  in an ideal process [51].

#### 4. Conclusion

Various flower-like  $\text{BiOBr}_x\text{Cl}_{1-x}$  solid solutions were successfully synthesized via a simple precipitation method. The microstructure of the flower-like microspheres depended on the molar ratios of Br/Cl. A Persian buttercup-like nanostructure was formed for Br/Cl = 1.5.  $\text{BiOBr}_{0.6}\text{Cl}_{0.4}$  has reduced band-gap and suitable band-edge positions for  $\text{CO}_2$  photoreduction. The  $\text{BiOBr}_{0.6}\text{Cl}_{0.4}$  solid solution showed an enhanced photocatalytic  $\text{CO}_2$  reduction activity compared with  $\text{BiOBr}$  or  $\text{BiOCl}$ , which was mainly attributed to the unique Persian buttercup-like nanostructure solid solutions with superior charge-carrier separation ability and suitable band-edge positions. The correlation between the structure and photocatalytic activity of the  $\text{BiOBr}_x\text{Cl}_{1-x}$  suggests a new strategy to design and prepare highly efficient photocatalysts for a wide range of applications.

#### Acknowledgements

This work is financially supported by the National Natural Science Foundation of China (Grants No. 21673042, 21673043), the Natural Science Foundation of Fujian Province of PR China (2017J01411), and the Technology Project of Education Office of Fujian Province of PR China (JAT160045).

#### Appendix A. Supplementary data

Supplementary material related to this article can be found, in the online version, at doi:<https://doi.org/10.1016/j.apcatb.2018.11.020>.

#### References

- [1] W. Zhu, R. Michalsky, Ö. Metin, H. Lv, S. Guo, C.J. Wright, X. Sun, A.A. Peterson, S. Sun, J. Am. Chem. Soc. 135 (2013) 16833–16836.
- [2] H. Rao, L.C. Schmidt, J. Bonin, M. Robert, Nature 548 (2017) 74.
- [3] S.R. Lingampalli, M.M. Ayyub, C.N.R. Rao, ACS Omega 2 (2017) 2740–2748.
- [4] S.M. Kim, P.M. Abdala, M. Broda, D. Hosseini, C. Copéret, C. Müller, ACS Catal. 8 (2018) 2815–2823.
- [5] M. Zhou, S. Wang, P. Yang, C. Huang, X. Wang, ACS Catal. 8 (2018) 4928–4936.
- [6] F. Sastre, A.V. Puga, L. Liu, A. Corma, H. García, J. Am. Chem. Soc. 136 (2014) 6798–6801.
- [7] H. Xu, S. Ouyang, P. Li, T. Kako, J. Ye, ACS Appl. Mater. Interfaces 5 (2013) 1348.
- [8] K. Li, B. Peng, T. Peng, ACS Catal. 6 (2016) 7485–7527.
- [9] D. Chen, X. Zhang, A.F. Lee, J. Mater. Chem. A 3 (2015) 14487–14516.
- [10] L. Wang, L. Wang, X. Liu, H. Wang, W. Zhang, Q. Yang, J. Ma, X. Dong, S.J. Yoo, J.G. Kim, Angew. Chem. Int. Edit. 57 (2018) 6104–6108.
- [11] S. Sato, T. Arai, T. Morikawa, Inorg. Chem. 54 (2015) 5105–5113.
- [12] B. Wang, X. Wang, L. Lu, C. Zhou, Z. Xin, J. Wang, X. Ke, G. Sheng, S. Yan, Z. Zou, ACS Catal. 8 (2018) 516–525.
- [13] D. Wu, L. Ye, A. Ho, Y. Yin, P.K. Wong, Catal. Sci. Technol. 7 (2017) 265–271.
- [14] X.Y. Kong, W. Lee, W.J. Ong, S.P. Chai, A.R. Mohamed, Chemcatchem 8 (2016) 3074–3081.
- [15] Z. Ma, P. Li, L. Ye, Y. Zhou, F. Su, C. Ding, H. Xie, Y. Bai, P.K. Wong, J. Mater. Chem. A 5 (2017) 24995–25004.
- [16] L. Zhang, W. Wang, D. Jiang, E. Gao, S. Sun, Nano Res. 8 (2015) 821–831.
- [17] J. Jin, Y. Wang, T. He, RSC Adv. 5 (2015) 100244–100250.
- [18] Q. Li, Z. Guan, D. Wu, X. Zhao, S. Bao, B. Tian, J. Zhang, ACS Sustain. Chem. Eng. 5 (2017) 6958–6968.
- [19] X. Wu, Y.H. Ng, L. Wang, Y. Du, S.X. Dou, R. Amal, J. Scott, J. Mater. Chem. A 5 (2017) 8117–8124.
- [20] M. Gao, D. Zhang, X. Pu, M. Li, Y.M. Yu, J.J. Shim, P. Cai, S.I. Kim, H.J. Seo, J. Am. Ceram. Soc. 98 (2015) 1515–1519.
- [21] S. Liang, M. He, J. Guo, J. Yue, X. Pu, B. Ge, W. Li, Sep. Purif. Technol. 206 (2018)

69–79.

[22] H. Gnayem, Y. Sasson, *ACS Catal.* 3 (2013) 186–191.

[23] X. Zhang, L. Wang, C. Wang, W. Wang, Y. Chen, Y. Huang, W. Li, Y. Feng, H. Yu, *Chem-Eur. J.* 21 (2015) 11872–11877.

[24] Y. Liu, W. Son, J. Lu, B. Huang, Y. Dai, M. Whangbo, *Chem-Eur. J.* 17 (2011) 9342–9349.

[25] D. Sun, J. Li, Z. Feng, L. He, B. Zhao, T. Wang, R. Li, S. Yin, T. Sato, *Catal. Commun.* 51 (2014) 1–4.

[26] Y. Peng, J. Xu, T. Liu, Y. Mao, *Crystengcomm* 19 (2017) 6473–6480.

[27] S. Wang, X. Hai, X. Ding, K. Chang, Y. Xiang, X. Meng, Z. Yang, H. Chen, J. Ye, *Adv. Mater.* 29 (2017) 1701774.

[28] J. Di, J. Xia, M. Ji, B. Wang, X. Li, Q. Zhang, Z. Chen, H. Li, *ACS Sustain. Chem. Eng.* 4 (2015) 136–146.

[29] M.N. Shaddad, D. Cardenas-Morcoso, P. Arunachalam, M. García-Tecedor, M.A. Ghanem, J. Bisquert, A. Al-Mayouf, S. Gimenez, *J. Phys. Chem. C* 122 (2018) 11608–11615.

[30] F. Tian, C. Liu, *J. Phys. Chem. B* 110 (2006) 17866–17871.

[31] P.A. Hernley, S.A. Chavez, J.P. Quinn, S. Linic, *ACS Photonics* 4 (2017) 979–985.

[32] B. Xu, Y. An, Y. Liu, X. Qin, X. Zhang, Y. Dai, Z. Wang, P. Wang, M. Whangbo, B. Huang, *J. Mater. Chem. A* 5 (2017) 14406–14414.

[33] M. Li, J. Zhang, H. Gao, F. Li, S. Lindquist, N. Wu, R. Wang, *ACS Appl. Mater. Interface* 8 (2016) 6662–6668.

[34] H. Xu, X. Han, Q. Tan, K. Wu, S. Qi, *Front. Mater. Sci.* 11 (2017) 120–129.

[35] J. Resasco, H. Zhang, N. Kornienko, N. Becknell, H. Lee, J. Guo, A.L. Briseno, P. Yang, *ACS Central. Sci.* 2 (2016) 80–88.

[36] S.Y. Gurudayal, M.H. Chiam, P.S. Kumar, H.L. Bassi, J. Barber Seng, L.H. Wong, *ACS Appl. Mater. Interface* 6 (2014) 5852–5859.

[37] L. Wang, D. Han, S. Ni, W. Ma, W. Wang, L. Niu, *Chem. Sci.* 6 (2015) 6632–6638.

[38] Y. Bai, L. Ye, T. Chen, P. Wang, L. Wang, X. Shi, P.K. Wong, *Appl. Catal. B: Environ.* 203 (2017) 633–640.

[39] T. Zhang, M. Liu, Y. Meng, B. Huang, X. Pu, X. Shao, *Sep. Purif. Technol.* 206 (2018) 149–157.

[40] J. Wang, L. Zhang, W. Fang, J. Ren, Y. Li, H. Yao, J. Wang, Z. Li, *ACS Appl. Mater. Int.* 7 (2015) 8631–8639.

[41] M.K. Barman, P. Mitra, R. Bera, S. Das, A. Pramanik, A. Parta, *Nanoscale* 9 (2017) 6791–6799.

[42] F.L. Formal, S.R. Pendlebury, M. Cornuz, S.D. Tilley, M. Grätzel, J.R. Durrant, *J. Am. Chem. Soc.* 136 (2014) 2564–2574.

[43] X. Jiao, Z. Chen, X. Li, Y. Sun, S. Gao, W. Yan, C. Wang, Q. Zhang, Y. Lin, Y. Luo, *J. Am. Chem. Soc.* 139 (2017) 7586–7594.

[44] H. Li, J. Shi, K. Zhao, L. Zhang, *Nanoscale* 6 (2014) 14168–14173.

[45] H. Li, J. Li, Z. Ai, F. Jia, L. Zhang, *Angew. Chem.* 130 (2018) 128–145.

[46] Y. Wu, B. Yuan, M. Li, W.H. Zhang, Y. Liu, C. Li, *Chem. Sci.* 6 (2014) 1873–1878.

[47] Q. Wu, Van dKR, J. Am. Chem. Soc. 134 (2012) 9369–9375.

[48] H. Li, J. Li, Z. Ai, F. Jia, L. Zhang, *Angew. Chem. Int. Edit.* 57 (2017) 122–138.

[49] S.N. Habisreutinger, L. Schmidt-Mende, J.K. Stolarczyk, *Angew. Chem. Int. Edit.* 52 (2013) 7372–7408.

[50] Y. Wang, Z. Zhang, L. Zhang, Z. Luo, J. Shen, H. Lin, J. Long, J.C.S. Wu, X. Fu, X. Wang, C. Li, J. Am. Chem. Soc. 140 (2018) 14595–14598, <https://doi.org/10.1021/jacs.8b09344>.

[51] L. Liang, X. Li, Y. Sun, Y. Tan, X. Jiao, H. Ju, Z. Qi, J. Zhu, Y. Xie, *Joule* 2 (2018) 1004–1016.